Chinese Chemical Letters 31 (2020) 71–76

Contents lists available at ScienceDirect

Chinese Chemical Letters

journal homepage: www.elsevier.com/locate/cclet

Communication

Synthesis of Z-scheme g-C_3N_4 nanosheets/Ag_3PO_4 photocatalysts with enhanced visible-light photocatalytic performance for the degradation of tetracycline and dye

Meng Ding[a], Juanjuan Zhou[a,b], Hongcen Yang[a], Ruya Cao[a], Shouwei Zhang[a], Minghui Shao[a], Xijin Xu[a,*]

[a] School of Physics and Technology, University of Jinan, Ji'nan 250022, China
[b] College of Optical and Electronic Technology, China Jiliang University, Hangzhou 310018, China

ARTICLE INFO

Article history:
Received 4 March 2019
Received in revised form 6 May 2019
Accepted 16 May 2019
Available online 17 May 2019

Keywords:
g-C_3N_4/Ag_3PO_4
Tetracycline
Photocatalytic activity
Photocurrent
Impedance

ABSTRACT

Graphene-like C_3N_4/Ag_3PO_4 photocatalysts are synthesized by calcination and solutions precipitating method. The obtained g-C_3N_4/Ag_3PO_4 composites display excellent photocatalytic activity for the degradation of methylene orange (MO), rhodamine B (RhB) and tetracycline (TC) under visible light irradiation. The solutions containing RhB (10 mg/L) and MO (10 mg/L) can be efficiently degraded within 15 min and 30 min. Especially, nearly 80% of TC (50 mg/L) is degraded within 20 min, which are much better than those of pure g-C_3N_4 nanosheets and Ag_3PO_4, implying that strong interaction and reasonable energy band alignment in the contact interface can effectively transfer the carries. Furthermore, the g-C_3N_4/Ag_3PO_4 composites exhibit the improved stability, and only a slight decrease is observed after three recycling runs. Moreover, the impact of inorganic ions and PH values on the degradation performance is rather small. The Z-scheme photocatalytic mechanism of the g-C_3N_4/Ag_3PO_4 composites based on the active species trapping experimental is proposed. This work demonstrates the promising applications of the g-C_3N_4/Ag_3PO_4 composites in environmental issues.

In recently years, water pollution caused by tetracycline (TC) and industry organism dye has induced serious threat to the health of human beings. Various technologies such as ion exchange, photocatalysis [1,2], adsorption [3], have been used to deal with water pollution problems. Among them, photocatalytic technology has been widely concerned because of its simple and low-cost and potential applications in environmental protection and energy production [4,5]. A large number of semiconductor metal oxide and sulphide photocatalysts, including TiO_2 [6,7], ZnO [8,9], WO_3 [10], CdS [11,12], In_2S_3 [13,14], Ag_3PO_4 [15], have been fabricated to develop efficient photocatalysts. As a photocatalyst, Ag_3PO_4 has been paid much more attention due to suitable band gap (2.36 eV) and the excellent photocatalytic property for the degradation of organic pollutants. However, some problems, including the high solubility, the photo-corrosion, instability and the fast recombination of photo-generated carriers, need to be solved. Many effective ways have been reported to improve the photocatalytic activity and stability of Ag_3PO_4, including size and morphology control, surface modification, constructing heterostructure/composite with other compounds [15,16]. Heterogeneous photocatalytic systems, such as Ag_3PO_4/Ag_2S [15], Ag_3PO_4/In_2S_3 [17], Ag_3PO_4/PANI [18], Ag_3PO_4/$CuBi_2O_4$ [16], carbon dots [19], are considered as effective strategies for the dispose of TC and dyes, which can suppress the photocorrsion, prompt migration and separation of the photogenerated electrons and holes.

Graphite carbon nitride (g-C_3N_4, 2.7 eV), as a nonmetallic polymeric material with high thermal, chemical stability and electronic properties, can have good visible light response [20,21], which has much more promising for practical application. Xia *et al.* [22] fabricated the multifunctional photocatalyst of Mn/g-C_3N_4/ZSM-4, then combined with vacuum ultraviolet irradiation to eliminate O_3 byproduct and enhance toluene degradation *via* ozone assisted catalytic oxidation. Zhang *et al.* [23] tuned the dimensions and structures of nitrogen doped carbon nanomaterials derived from sacrificial g-C_3N_4/metal–organic frameworks to enhance electrocatalytic oxygen reduction. Moreover, g-C_3N_4 nanosheets can be used as a coating material due to its flexibility. Chen *et al.* [24] reported that the stability and photocatalytic performance of ZnO could be enhanced by coating g-C_3N_4 nanosheets as shell layer, which could be attributed to the

* Corresponding author.
E-mail address: sps_xuxj@ujn.edu.cn (X. Xu).

https://doi.org/10.1016/j.cclet.2019.05.029
1001-8417/

hybridized effect and the core–shell structure induced by the match of lattice and energy level between the C_3N_4 shell and ZnO core. However, the photocatalytic efficiency of g-C_3N_4 is still not highly attributing to the high recombination rate of the photogenerated electron–hole pairs. To improve the separation efficiency of photogenerated carriers, heterojunction photocatalyst between g-C_3N_4 and other materials should be constructed. Considering the excellent photooxidation activity of Ag_3PO_4, g-C_3N_4/Ag_3PO_4 heterostructures have been fabricated and reported [25–29]. Liu *et al.* [29] reported the degradation of methylene blue (MB) over Ag_3PO_4@g-C_3N_4 hybrid core@shell composite, which presented the better photocatalytic activity. Ma *et al.* [30] reported nanocomposite of exfoliated bentonite/g-C_3N_4/Ag_3PO_4 for enhanced visible-light photocatalytic decomposition of RhB. However, the previously reported g-C_3N_4/Ag_3PO_4 composites still suffer the low efficiency and poor stability.

In this work, 2D g-C_3N_4 nanosheets were served as support to fabricate g-C_3N_4/Ag_3PO_4 composite photocatalyst by calcination and solutions precipitating method. Their photocatalytic activities are evaluated by the degradation of three different kinds of pollutants (MO, RhB, TC) under visible light irradiation. Moreover, the effects of pH and coexisting ions are also investigated. The photocurrent response and electrochemical impedance spectra (EIS) performance of the g-C_3N_4/Ag_3PO_4 heterostructure is also discussed, and the possible mechanism of the photocatalytic activity is also proposed.

The XRD patterns of the as-prepared samples are displayed in Fig. 1. For pure g-C_3N_4 nanosheets, two characteristic diffraction peaks at 13.2° and 27.6° are observed, which correspond to the (100) and (002) planes of g-C_3N_4 [31], respectively. For the bare Ag_3PO_4, all the diffraction peaks can be assigned to the cubic phase of Ag_3PO_4 without any impurities (JCPDS: 06-0505). Compared with bare Ag_3PO_4, the weak characteristic diffraction peaks of g-C_3N_4 are found in the XRD pattern of g-C_3N_4/Ag_3PO_4 composite, which demonstrate the existence of both g-C_3N_4 and Ag_3PO_4, further indicating that the successful formation of g-C_3N_4/Ag_3PO_4 binary heterojunction composite.

Fig. 2a shows that the as-fabricated C_3N_4 has sheet morphology with large size and very small thickness. Form Fig. 2b, it can be observed that Ag_3PO_4 particles have an irregular spherical morphology with smooth surface and a tendency to aggregate,

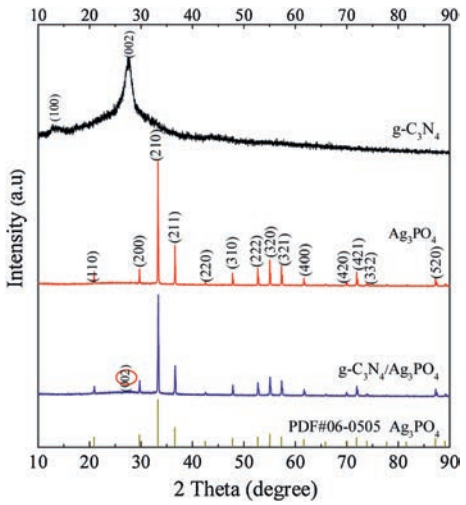

Fig. 1. XRD patterns of the as-prepared g-C_3N_4 nanosheets, Ag_3PO_4, g-C_3N_4/Ag_3PO_4 composite.

and the size of particles is about 0.1–0.7 μm. For g-C_3N_4/Ag_3PO_4 composite, Ag_3PO_4 particles are distinctly anchored on the surface of g-C_3N_4 nanosheets, also some particles are enwrapped with g-C_3N_4 nanosheets, as shown in Figs. 2c–e. The high-resolution TEM image of C_3N_4/Ag_3PO_4 composite in Fig. 2f clearly shows the crystalline lattice fringes with the interplanar distance of 0.239 nm, which corresponds to the (211) plane of cubic Ag_3PO_4 phase. Moreover, it confirms that g-C_3N_4 nanosheet can act as a support and surfactant to constrain Ag_3PO_4 particles in the composite. The elemental mappings in Fig. S1 (Supporting information) reveal the coexistence of five elements, including C, N, Ag, P and O. The uniform distributions of C and N elements among the sample indicate the presence of g-C_3N_4 nanosheets. Furthermore, the mapping images also verify that Ag, P and O elements form clusters with the uniform size and shape as SEM images confirmed, indicating that Ag_3PO_4 particles uniformly disperse on the surfaces of g-C_3N_4. The above-mentioned elements in g-C_3N_4/Ag_3PO_4 composite are also confirmed by EDX measurement (Fig. S1).

Five elements, C, N, Ag, P and O, can be observed in the survey spectrum in Fig. 3a, which is consistent with the result of EDS. For C 1s spectrum in Fig. 3b, two peaks at about 284.6 eV and 288.0 eV are present, which can be ascribed to sp^2 C—C bonds in graphitic or amorphous carbons and carbon atoms with three nitrogen atoms (C—N_3) bonds in g-C_3N_4, respectively [32]. The N 1s spectrum (Fig. 3c) can be deconvoluted into three peaks at 398.3 eV, 399.0 eV and 400.9 eV, respectively. The peak at 398.3 eV is attributed to sp^2-hybridized nitrogen (C=N—C), suggesting the existent of g-C_3N_4. The other two peaks located at 399.0 eV, 400.9 eV are tertiary nitrogen (N—$(C)_3$) groups and amino functions (C—N—H) [27,33], respectively. Three peaks at 530.86 eV, 531.74 eV, 532.92eV for O 1s in Fig. 3d are ascribed to O_2^- in Ag_3PO_4 [27], the surface OH-groups and the surface adsorbed H_2O molecules [19], respectively. Fig. 3e shows the binding energies of the Ag $3d_{5/2}$ and $3d_{3/2}$ peaks at 368.10 eV and 374.02 eV, which are usually ascribed to Ag^+ in Ag_3PO_4. Furthermore, a broad peak centered at 132.69 eV of the P 2p spectrum (Fig. 3f) is observed for the composite, which is in consistent with P^{+5} from PO_4^{3-} [19].

The UV–vis diffuse reflectance spectra of g-C_3N_4, Ag_3PO_4 and g-C_3N_4/Ag_3PO_4 in Fig. S2a (Supporting information) shows that the light absorption edges of pure g-C_3N_4 and Ag_3PO_4 are located at about 430 nm and 530 nm, corresponding to band gap of 2.88 eV and 2.45 eV, in consistent with the reported result [19]. After the combination of g-C_3N_4 with Ag_3PO_4, the band gap absorption edge of composite displays red shifted compared with g-C_3N_4, implying the enhanced absorption ability of the composite in the visible light region. Therefore, more light will be absorbed and more electrons and holes are generated for the g-C_3N_4/Ag_3PO_4 composite. Fig. S2b (Supporting information) exhibits the PL spectra of g-C_3N_4 and the g-C_3N_4/Ag_3PO_4 composite with the excitation at 350 nm. The PL intensity of g-C_3N_4/Ag_3PO_4 composite is weaker than the pure g-C_3N_4, which suggests that the combination of g-C_3N_4 with Ag_3PO_4 can effectively inhibit recombination of photoexcited electron-holes pairs.

To investigate the potential applicability of the composites, the photocatalytic properties of the samples were investigated by monitoring the degradation of MO, RhB and TC aqueous solution under visible light. As shown in Fig. 4a, the adsorption-desorption equilibrium between MO and photocatalysts will be reached within 90 min in the dark. 45.2% of MO (10 mg/L) will be adsorbed by g-C_3N_4/Ag_3PO_4 composites, which are far above those of pure g-C_3N_4 nanosheets and Ag_3PO_4 particles, suggesting that g-C_3N_4/Ag_3PO_4 composites have superior adsorptive ability. The blank experiment indicates that only little MO is degraded in the absence of photocatalyst, thus it can be negligible. Further, 95% of MO is

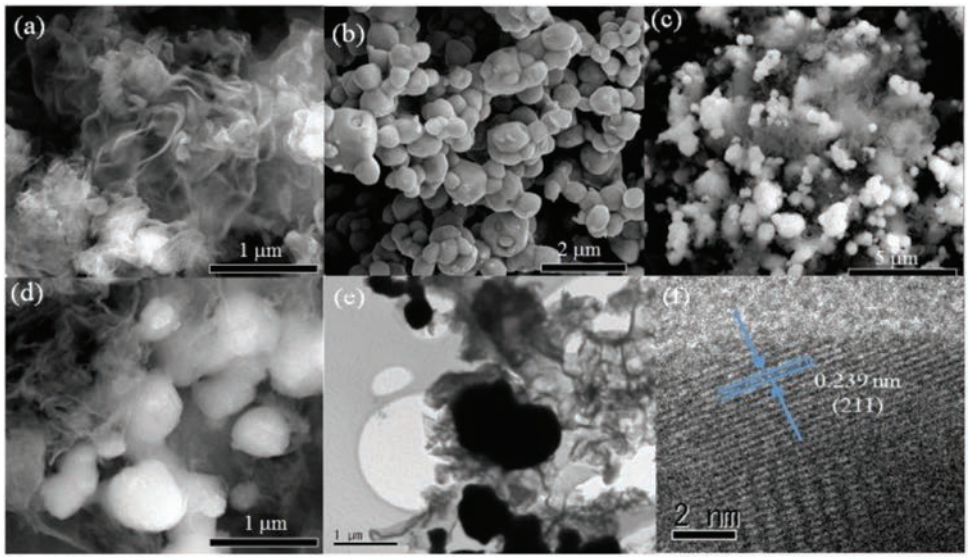

Fig. 2. SEM images of (a) bare g-C_3N_4 nanosheets, (b) Ag_3PO_4, (c, d) g-C_3N_4/Ag_3PO_4 composite. (e) TEM image and (f) high-resolution TEM image of g-C_3N_4/Ag_3PO_4 composite.

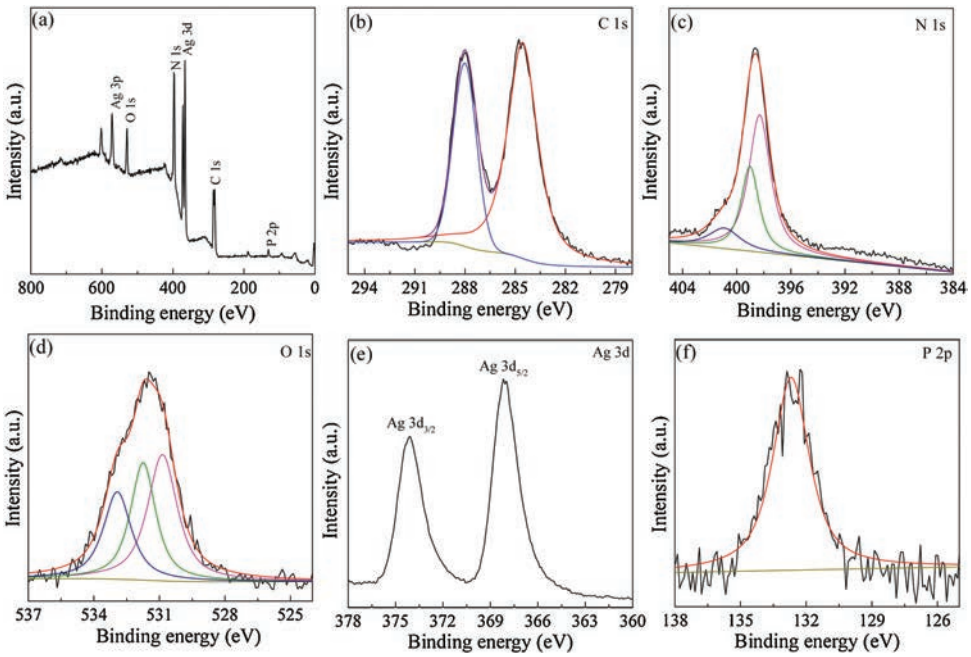

Fig. 3. (a) XPS survey spectrum, XPS spectra of (b) C 1s, (c) N 1s, (d) O 1s, (e) Ag 3d and (f) P 2p for g-C_3N_4/Ag_3PO_4 composite.

degraded in the presence of g-C_3N_4/Ag_3PO_4 composite after 30 min. In comparison, only 10.0% and 39.1% are degraded for the g-C_3N_4 nanosheets and Ag_3PO_4 particles, respectively. After adsorption equilibrium for 60 min, more than 28.6% of RhB is adsorbed by g-C_3N_4/Ag_3PO_4 composite, as shown in Fig. 4c. The adsorptions of RhB on pure Ag_3PO_4 and pure g-C_3N_4 are 3.3% and 35.6%, respectively. More than 96% of RhB (10 mg/L) is degraded in the presence of g-C_3N_4/Ag_3PO_4 composite under visible irradiation for 15 min. The experiment results further prove that the g-C_3N_4/Ag_3PO_4 composites have superior adsorptive and photodegradation ability compared with the pure Ag_3PO_4 and pure g-C_3N_4 nanosheets. To further understand the reaction kinetics of the MO and RhB degradation catalyzed by various photocatalysts, the experimental data are fitted by a pseudo-first-order kinetics model as follows [16]:

$$\ln(c/c_0) = -kt$$

where C_0 represents the initial concentration of dye and C refers to the concentration of dye at different irradiation times t, and k is the reaction rate constant. Obviously, the calculated k for the degradation of MO and RhB over g-C_3N_4/Ag_3PO_4 composite is larger than those calculated for the reactions over pure g-C_3N_4 nanosheets and Ag_3PO_4, as shown in Figs. 4b and d. Especially, the k value for the degradation of MO over g-C_3N_4/Ag_3PO_4 composite (0.1187 min^{-1}) is about 7.67 folds compared with that of Ag_3PO_4 (0.0155 min^{-1}). Likewise, the k value for the degradation of RhB

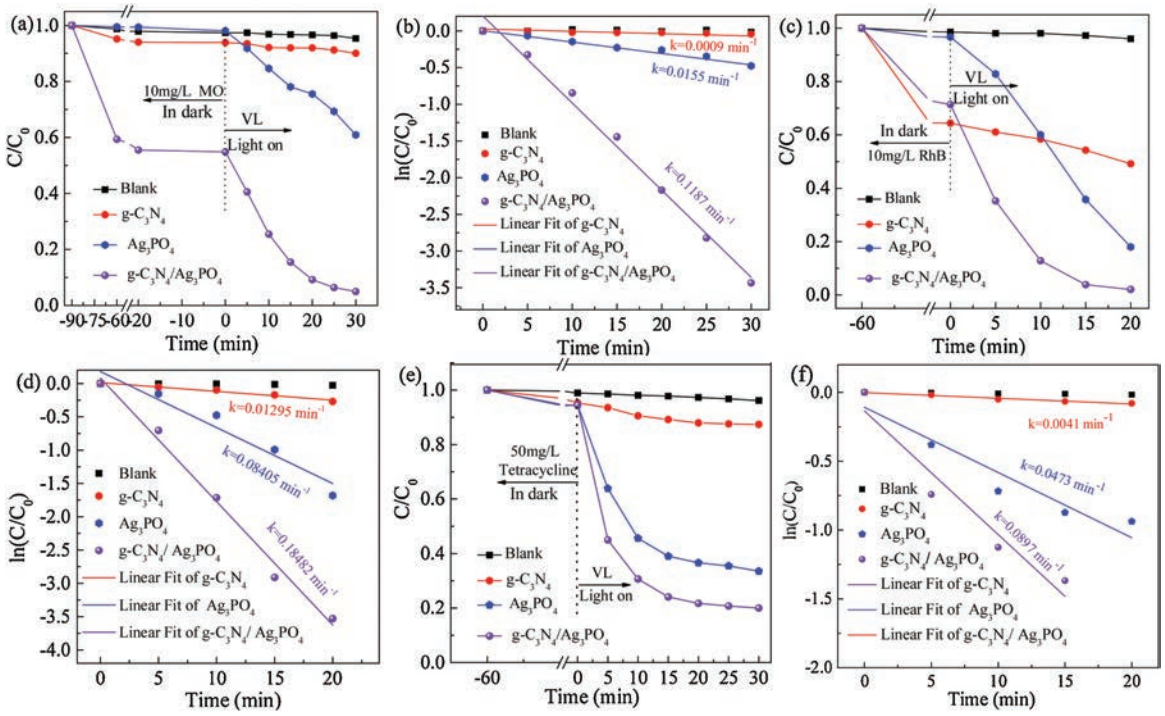

Fig. 4. (a) Relative concentration (C/C_0) of MO (10 mg/L) *versus* time under visible light irradiation. (b) The corresponding plots of $\ln(C/C_0)$ *versus* time of (a). (c) Relative concentration (C/C_0) of RhB (10 mg/L) *versus* time. (d) the corresponding plots of $\ln(C/C_0)$ *versus* time of (c). (e) Photocatalytic degradation of 50 mg/L TC by as-fabricated photocatalysts. (f) The pseudo-first-order reaction kinetics for the degradation of 50 mg/L TC with prepared samples.

over g-C_3N_4/Ag_3PO_4 composite (0.18482 min^{-1}) is about 2.20 folds compared with that of Ag_3PO_4 (0.08405 min^{-1}). To further understand the photocatalytic activity of the fabricated samples, the degradations of TC are performed. As seen from Fig. 4e, the adsorption-desorption equilibrium between TC and photocatalysts can be achieved within 60 min in the dark. Meanwhile, the adsorption ability of g-C_3N_4/Ag_3PO_4 composite exhibits higher compared with that of pure g-C_3N_4 nanosheets and Ag_3PO_4 particles, which is consistent with the result of degradations of MO and RhB. Moreover, the blank experiment suggests that the self-degradation of TC can be ignored, and pure g-C_3N_4 nanosheets and Ag_3PO_4 show poor photocatalytic activities, in which merely about 12.6% and 65.8% of TC are degraded in 30 min under visible light irradiation, respectively. While for g-C_3N_4/Ag_3PO_4 composite, nearly 80% of TC can be degraded within 30 min. Fig. 4f shows the preudo-first-order reaction kinetics for the degradation of 50 mg/L TC with prepared samples, which display that the *k* value for the degradation of TC over g-C_3N_4/Ag_3PO_4 composite (0.0897 min^{-1}) is about 1.9 folds and 21.8 folds compared with those of Ag_3PO_4 (0.0473 min^{-1}) and g-C_3N_4 nanosheets (0.0041 min^{-1}), respectively. The experimental results suggest that the introduction of the Ag_3PO_4 on the g-C_3N_4 nanosheets facilitates photogenerated carrier, thus significantly improving the photocatalytic activity.

In the actual wastewater system, there are some coexisting ions, and the pH value are different, so the impact of inorganic ions and pH values on the degradation performance should be considered [34,35]. For mimic natural wastewater, various inorganic ions with the concentration of 0.1 mol/L, including Na^+, Cl^-, SO_4^{2-}, NO_3^-, CO_3^{2-}, are added to the TC solution to investigate the catalytic efficiency of g-C_3N_4/Ag_3PO_4 catalytic system, and the results are shown in Fig. 5a. No obvious difference can be observed in the degradation curves of the TC solutions containing Na_2CO_3, $NaNO_3$, Na_2SO_4, suggesting the universal photocatalytic effects of g-C_3N_4/Ag_3PO_4 composite in different environment. However, the catalytic efficiency toward TC degradation decreases a little in the presence of NaCl. The photocatalyst g-C_3N_4/Ag_3PO_4 after reaction is further characterized with XRD as displayed in Fig. S3 (Supporting information), in which no diffraction peaks of g-C_3N_4/Ag_3PO_4 can be observed, suggesting that the transformation of g-C_3N_4/Ag_3PO_4 composite photocatalyst to other substances with the introduction of NaCl. The appearance of characteristic peaks of AgCl (JCPDS: 31-1238) imply that the crystal structure of g-C_3N_4/Ag_3PO_4 has been transformed into AgCl. Therefore, photocatalytic activity is reduced because of the destroyed crystal structure of Ag_3PO_4 [36]. The influence of pH values on the degradation toward TC is displayed in Fig. 5b, when the pH values are within the range of 2.87–9.24, the g-C_3N_4/Ag_3PO_4 composite show excellent photodegradation activities towards TC, only the photodegradation efficiency at the pH values of 9.24 reduces a little. The results suggest that g-C_3N_4/Ag_3PO_4 can be used as an efficient photocatalyst for practical application in wastewater treatment.

In order to study the photocatalytic stability of the as-fabricated samples, recycle experiments of MO degradation over g-C_3N_4 nanosheets, Ag_3PO_4 and the g-C_3N_4/Ag_3PO_4 composite were carried out, as shown in Fig. 6a. For the bare Ag_3PO_4, the photocatalytic efficiency decreases from 64.5% to 29.1% after five cycles, indicating the bare Ag_3PO_4 photocatalyst is unstable. The significant reduction of the photocatalytic performance of Ag_3PO_4 can be attributed to the partial reduction of Ag^+ into Ag^0 by photogenerated electrons [35]. In contrast, the degradation of g-C_3N_4/Ag_3PO_4 composite remains high (~93%) across the repeated cycles, with a slight decrease to 88% observed after five recycling runs. The effective energy level structure facilitates the separation of the electron-hole pairs quickly, thus obviously improving the photoactivity and photostability of catalyst. The result is in accord with the analysis of PL (Fig. S2 in Supporting information), transient photocurrent responses (Fig. S4a in

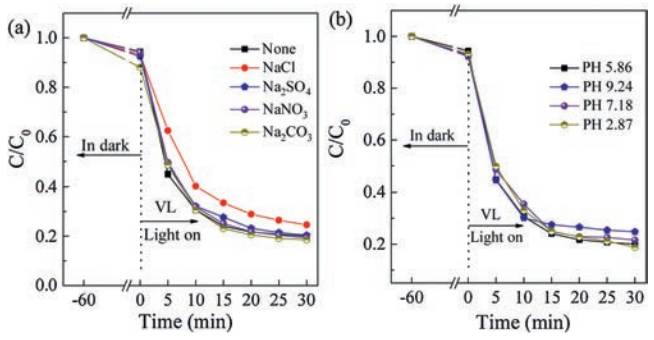

Fig. 5. (a) Photodegradation curves of TC (50 mg/L) with different inorganic salts. (b) Photodegradation curves of TC at different pH condition using g-C_3N_4/Ag_3PO_4 composite as photocatalysts.

Supporting information) and EIS measurement (Fig. S4b in Supporting information). Furthermore, the XRD of the as-fabricated is compared with that used g-C_3N_4/Ag_3PO_4 composite after 5 cycles, as Fig. 6b shows. After photocatalytic reaction, no crystal structure variation of the composite is observed. A rather weak characteristic diffraction peaks at 38.1° is observed and attributed to the (111) crystal planes of metallic silver, indicating that only a small quantity of Ag generated in the photodegradation process. The appearance of a small amount of Ag serves as the transmission bridge of carrier, thus the carrier transfer rate and the separation of electron-hole pairs can be improved by the Schottky barriers at the metal-semiconductor interfaces. Furthermore, the localized surface plasmon resonance of Ag nanoparticles on catalyst can also promote the photocatalytic efficiency. The results indicate that high photocatalytic efficiency and stability of the g-C_3N_4/Ag_3PO_4 composite, which are important attribution for their practical applications in real-life for eliminating organic pollutants from wastewater.

As is known that the three major reactive species, superoxide radical ($^{\bullet}O_2^-$), hole (h^+) and hydroxyl radical ($^{\bullet}OH$) play important role in photocatalytic reaction process. In order to investigate the dominant active species in the photocatalytic process, the trapping experiments were carried out. As displayed in Fig. S5 (Supporting information), the photocatalytic activities of g-C_3N_4/Ag_3PO_4 composite toward the degradation of MO are investigated in the presence of benzoquinone (BZQ), ethylenediaminetetraacetic acid (EDTA) and isopropanol (IPA) employed to act as $^{\bullet}O_2^-$, h^+ and $^{\bullet}OH$ scavengers, respectively. Obviously, the introduction of BZQ and EDTA into the photocatalyst can basically affect the photodegradation efficiencies of MO, the photocatalytic degradation is

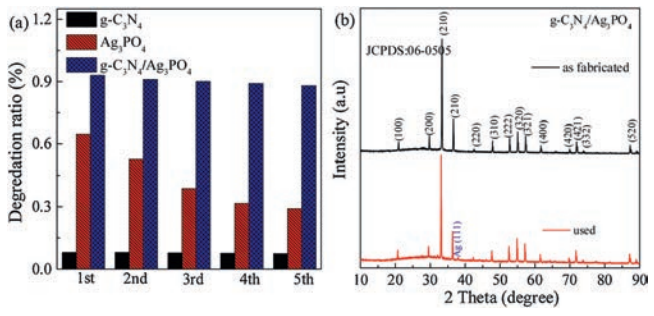

Fig. 6. (a) Recycling tests for the photocatalytic MO degradation in the presence of g-C_3N_4/Ag_3PO_4 composite photocatalyst under visible-light irradiation. (b) XRD pattern of the as-fabricated and the used g-C_3N_4/Ag_3PO_4 composite.

greatly quenched, which suggests that $^{\bullet}O_2^-$ and h^+ are the main reactive species in the g-C_3N_4/Ag_3PO_4 composite photocatalytic process. In contrast, the photocatalytic degradation of MO is inhibited slightly by introducing IPA, suggesting that the $^{\bullet}OH$ also has small effect on the photocatalytic efficiency.

On the basis of the above experimental results and characterization analysis, a possible photocatalytic mechanism of the g-C_3N_4/Ag_3PO_4 composite photocatalyst is proposed to follow a Z-scheme mechanism, as illustrated in Fig. 7. According to the previous reports [16,28,29,37,38], the valence band (VB) and conduction band (CB) potentials of Ag_3PO_4 are about 2.67 and 0.27 eV, which is both more positive than that of g-C_3N_4 (1.60 and −1.15 eV), respectively. Under visible light irradiation, the electrons in the VB of both g-C_3N_4 and Ag_3PO_4 are excited to the CB, leaving holes in the VB. The CB of Ag_3PO_4 is more negative than the Fermi level of metallic Ag, and the VB of g-C_3N_4 is more positive than the Fermi level of Ag, thus the photo-excited electrons in the CB of Ag_3PO_4 is more likely to be transferred to the metallic silver. Meanwhile, the photogenerated holes in VB of g-C_3N_4 are transferred to Ag and combined with electrons. Then, the electrons left in CB of g-C_3N_4 can combine with the dissolved oxygen molecules and produce the superoxide radical anions ($^{\bullet}O_2^-$), which play an important role in overall photocatalytic reaction. In addition, the photogenerated holes in VB of Ag_3PO_4 could directly oxidize dye. Of course, part of photogenerated holes can combine with OH^- to produce active $^{\bullet}OH$. Thus, the photocatalytic activity of g-C_3N_4/Ag_3PO_4 composite are mainly attributed to the generated $^{\bullet}O_2^-$ and h^+ active species, meanwhile, parts of $^{\bullet}OH$ can also degrade dye and TC. Therefore, Ag nanoparticles existed in the interface of g-C_3N_4 and Ag_3PO_4 might act as a charge transmission bridge to efficiently improve the separation of electron-hole pairs. Considering strong absorption of the degradation substrates (MO and RhB) in the region of the illumination, the photosensitization also plays certain function in the photocatalytic process. Dyes can be excited by visible light and produce the excited state of the dye*, electron will inject from the adsorbed dye* species to the semiconductor conduction band (and/or surface states), also the oxidized dye species (dye+) can be produced when electrons are lost. The injected electron can combine with the surface-adsorbed O_2 molecules to produce the $^{\bullet}O_2^-$, in competition with back electron transfer to the dye^+ radical cation. However, the former process is usually two/three-order faster [39–41]. The superoxide radical anions can be involved in photocatalytic degradation, thus the photosensitization partially works in the photocatalytic process.

In summary, g-C_3N_4/Ag_3PO_4 photocatalysts were successfully constructed by *in situ* deposition of Ag_3PO_4 onto 2D g-C_3N_4 nanosheets through precipitating method. The photocatalytic results showed that the g-C_3N_4/Ag_3PO_4 composite had obviously superior photocatalytic activity and photostability over that of pure Ag_3PO_4 particles and g-C_3N_4 nanosheets for the photodegradation of MO, RhB and TC under visible light irradiation. The improved photocatalytic activity can be ascribed to the efficient separation of photoinduced electron–hole pairs. The photocatalytic process of the g-C_3N_4/Ag_3PO_4 photocatalysts were further supported by transient photocurrent response, PL spectrum, active species trapping experiment results. The work could supply insight into fabricating novel photocatalysts with high efficiency and reusability for important applications in elimination organic pollutants from wastewater.

Acknowledgments

This work was financially supported by the National Natural Science Foundation of China (Nos. 61504048, 51672109, 21707043), Natural Science Foundation of Shandong Province for Excellent Young Scholars (Nos. ZR2016JL015, ZR2017BEE005).

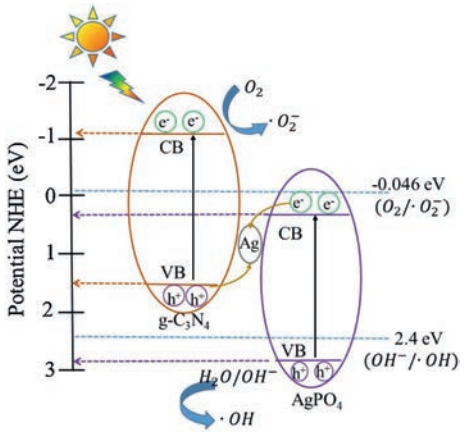

Fig. 7. Schematic diagram of photogenerated electron-hole separation process between g-C_3N_4 and Ag_3PO_4.

Appendix A. Supplementary data

Supplementary material related to this article can be found, in the online version, at doi:https://doi.org/10.1016/j.cclet.2019.05.029.

References

[1] Z.B. Yu, Y.P. Xie, G. Liu, et al., J. Mater. Chem. A 1 (2013) 2773–2776.
[2] L. Zhang, L. Du, X. Yu, et al., ACS Appl. Mater. Interface 6 (2014) 3623–3629.
[3] S. Zhang, M. Zeng, W. Xu, et al., Dalton Trans. 42 (2013) 7854–7858.
[4] W. He, G. Zhao, P. Sun, et al., Nano Energy 56 (2019) 207–215.
[5] C. Wang, P. Sun, G. Qu, J. Yin, X.J. Xu, Chin. Chem. Lett. 29 (2018) 1731–1740.
[6] R. Wang, G. Jiang, Y. Ding, et al., ACS Appl. Mater. Interface 3 (2011) 4154–4158.
[7] S. Rhatigan, M. Nolan, Chin. Chem. Lett. 29 (2018) 757–764.
[8] S. Martha, K.H. Reddy, K.M. Parida, J. Mater. Chem. A 2 (2014) 3621–3631.
[9] P. Huo, J. Li, Z. Ye, et al., Chin. Chem. Lett. 28 (2017) 2259–2262.
[10] Y. Zhang, D.F. Zhang, X.Y. Xu, B.S. Zhang, Chin. Chem. Lett. 29 (2019) 1350–1354.
[11] F.X. Xiao, J. Miao, B. Liu, J. Am. Chem. Soc. 136 (2014) 1559–1569.
[12] M. Ding, N. Yao, C. Wang, et al., Nanoscale Res. Lett. 11 (2016) 205.
[13] X. Fu, X. Wang, Z. Chen, et al., Appl. Catal. B: Environ. 95 (2010) 393–399.
[14] W. Qiu, M. Xu, X. Yang, et al., J. Mater. Chem. 21 (2011) 13327–13333.
[15] J. Tian, T. Yan, Z. Qiao, et al., Appl. Catal. B: Environ. 209 (2017) 566–578.
[16] W. Shi, F. Guo, S. Yuan, Appl. Catal. B: Environ. 209 (2017) 720–728.
[17] T. Yan, J. Tian, W. Guan, et al., Appl. Catal. B: Environ. 202 (2017) 84–94.
[18] L. Liu, L. Ding, Y. Liu, et al., Appl. Catal. B: Environ. 201 (2017) 92–104.
[19] X. Miao, X. Yue, Z. Ji, et al., Appl. Catal. B: Environ. 227 (2018) 459–469.
[20] X. Bai, L. Wang, R. Zong, Y. Zhu, J. Phys. Chem. C 117 (2013) 9952–9961.
[21] L. Sun, Y. Qi, C.J. Jia, Z. Jin, W. Fan, Nanoscale 6 (2014) 2649–2659.
[22] D. Xia, W. Xu, L. Hu, et al., J. Hazard. Mater. 349 (2018) 91–100.
[23] R. Wang, T. Yan, L. Han, et al., J. Mater. Chem. A 6 (2018) 5752–5761.
[24] D. Chen, K. Wang, D. Xiang, et al., Appl. Catal. B: Environ. 147 (2014) 554–561.
[25] S. Kumar, T. Surendar, A. Baruah, V. Shanker, J. Mater. Chem. A 1 (2013) 5333–5340.
[26] F.J. Zhang, F.Z. Xie, S.F. Zhu, et al., Chem. Eng. J. 228 (2013) 435–441.
[27] H. Katsumata, T. Sakai, T. Suzuki, S. Kaneco, Ind. Eng. Chem. Res. 53 (2014) 8018–8025.
[28] X.X. Chen, X.T. Huang, Z.G. Yi, Chem. Eur. J. 20 (2014) 17590–17596.
[29] L. Liu, Y. Qi, J. Lu, et al., Appl. Catal. B: Environ. 183 (2016) 133–141.
[30] J. Ma, D. Huang, W. Zhang, et al., Chemosphere 162 (2016) 269–276.
[31] S. Zhang, H. Gao, Y. Huang, et al., Environ. Sci. Nano 5 (2018) 1179–1190.
[32] J. Li, M. Zhou, Z. Ye, et al., RSC Adv. 5 (2015) 91177–91189.
[33] H. Yang, S. Zhang, R. Cao, et al., Sci. Rep. 7 (2017) 8686.
[34] S. Zhang, Q. Fan, H. Gao, et al., J. Mater. Chem. A 4 (2016) 1414–1422.
[35] Y. Lin, S. Wu, C. Yang, M. Chen, X. Li, Appl. Catal. B: Environ. 245 (2019) 71–86.
[36] T. Cai, Y. Liu, L. Wang, et al., Appl. Catal. B: Environ. 208 (2017) 1–13.
[37] L. Zhou, W. Zhang, L. Chen, H. Deng, J. Colloid Interface Sci. 487 (2017) 410–417.
[38] X. Li, T. Wan, J. Qiu, et al., Appl. Catal. B: Environ. 217 (2017) 591–602.
[39] T. Wu, G. Liu, J. Zhao, H. Hidaka, N. Serpone, J. Phys. Chem. B 102 (1998) 5845–5851.
[40] J. Hu, W. Fan, W. Ye, C. Huang, X. Qiu, Appl. Catal. B: Environ. 158–159 (2014) 182–189.
[41] C. Michelin, N. Hoffmann, ACS Catal. 8 (2018) 12046–12055.